

Ultrasensitive Macrocyclic Membranes for Pharmaceutical Ingredients Separation in Organic Solvents

Received: 31 March 2024

Accepted: 12 August 2024

Published online: 21 August 2024

 Check for updatesBanan Alhazmi^{1,6}, Gergo Ignacz^{2,3,6}, Maria Di Vincenzo¹,
Mohamed Nejib Hedhili⁴, Gyorgy Szekely^{1,2,3}  & Suzana P. Nunes^{1,2,5} 

Separations are core processes in the chemical and pharmaceutical industries. Several steps of fractionation and purification of multicomponent mixtures are required. Membrane technology can operate at fair temperatures, saving energy and processing sensitive compounds. However, breakthroughs require high stability and selectivity beyond those available today. Here, we propose membranes constituted by fully crosslinked crown ethers using interfacial polymerization. The 24 nm-thick nanofilms on robust porous supports exhibit up to 90% higher selectivity than commercially available membranes, with a 90% increase in solvent permeance. The membranes are tested with a complex mixture of structurally diverse solutes containing active pharmaceutical ingredients. The membranes are effective for the total retention and concentration of active pharmaceutical ingredients with molecular weights around 800 g mol⁻¹. The ability to distinguish between smaller molecules in the range between 100 and 370 g mol⁻¹ is confirmed with high separation factors, which could provide a significant advance for the pharmaceutical industry.

Separation processes are indispensable in the chemical and pharmaceutical industries, addressing crucial functions such as high-value chemical concentration, purification, solvent exchange and recovery, and catalyst recycling¹. These processes currently account for 40–70% of both capital and operating costs. Efficient and cost-effective alternatives to energy-intensive methods like distillation and evaporation are urgently needed^{2,3}. Organic solvent nanofiltration (OSN) and reverse osmosis (OSRO) have emerged as viable membrane-based solutions for molecular separations and purification in organic solvents. Despite its environmental and economic advantages, the current technology faces challenges associated with a permeability-

selectivity tradeoff stemming from the use of conventional amorphous polymers⁴. These polymers, though highly processable and scalable, result in membranes with heterogeneous networks and structures, leading to non-uniform transport paths and ineffective control over selectivity⁵. Several strategies have, therefore, been proposed to address these challenges by tailoring the polymer structure at the molecular level to promote uniform porosity for effective molecular separations.

Thin-film composite (TFC) membranes are an important class of polymer membranes evolved for water desalination, mainly fabricated by the interfacial polymerization reaction between *m*-

¹Environmental Science and Engineering Program, Biological and Environmental Science and Engineering Division (BESE), King Abdullah University of Science and Technology (KAUST), Thuwal, Saudi Arabia. ²Chemical Engineering Program, Physical Science and Engineering Division (PSE), King Abdullah University of Science and Technology (KAUST), Thuwal, Saudi Arabia. ³Advanced Membranes and Porous Materials Center, Physical Science and Engineering Division (PSE), King Abdullah University of Science and Technology (KAUST), Thuwal, Saudi Arabia. ⁴Imaging and Characterization Laboratory, King Abdullah University of Science and Technology (KAUST), Thuwal, Saudi Arabia. ⁵Chemistry Program, Physical Science and Engineering Division (PSE), King Abdullah University of Science and Technology (KAUST), Thuwal, Saudi Arabia. ⁶These authors contributed equally: Banan Alhazmi, Gergo Ignacz.

✉ e-mail: gyorgy.szekely@kaust.edu.sa; suzana.nunes@kaust.edu.sa

phenylenediamine and trimesoyl chloride⁶. The process has been adapted for OSN to produce freestanding polyamide nanofilms with high solvent permeance⁷. Efforts to enhance solvent permeance have also explored the introduction of semi-flexible microporosity and connectivity of intermolecular voids into polymer membranes by using contorted and rigid building blocks^{8,9}. However, achieving precise molecular sieving and overcoming the permeability-selectivity tradeoff necessitate membrane materials with well-defined and tunable porous structures. Microporous organic materials, such as metal-organic frameworks, covalent organic frameworks, and porous organic cages, may improve the permeability and selectivity of membranes^{10,11}. However, the fabrication of crystalline materials without defects remains difficult and is highly challenging to scale up¹¹. Furthermore, an extensive study has indicated that ultra-high permeance may limit overall membrane system productivity due to non-ideal effects arising from concentration polarization and pressure drops, emphasizing the importance of prioritizing membrane selectivity¹².

Recently, macrocyclic compounds with intrinsic cavities, such as cyclodextrin, calixarene, cucurbituril, pillaranes, and triangle amines, have garnered interest in membrane applications for selective separations in organic solvents^{13–16}. Leveraging their unique porous structure, diverse chemical functionalities, and molecular recognition capability, these macrocycles have been covalently incorporated into selective nanofilms through interfacial polymerization. This approach has proven effective in forming stable defect-free nanofilms that retain the intrinsic characteristics of the macrocycles without leaching out during operation. Notably, efforts to optimize the reaction conditions for functionalized cyclodextrin have shown excellent nanofiltration performance with high permeance for both non-polar and polar solvents, attributed to the amphiphilic nature of the macrocycle^{15,17}. These membranes also exhibit good selectivity for molecules of similar size but different shapes. Most recently, functionalized cyclodextrins with differentiated reactivities, generating ordered sub-nanometer channels across ultrathin films, have demonstrated improved performance compared to their disordered counterparts¹⁸. In addition, our group proposed triangle amine-based membranes that had interesting selectivity for racemic mixtures of amino acids, with promising results for tryptophan¹⁴.

However, the success of this strategy is contingent upon addressing the inherent limitations of macrocycles, such as their restricted solubility and reactivity, which can impact the efficiency of the interfacial polymerization process. Crown ethers have gained prominence as complexing agents since their discovery¹⁹. These cyclic polyethers engage in ion-dipole interactions with positively charged metal or ammonium ions. In tailoring membranes, crown ethers have been employed as additives to regulate the diffusion rate of the monomers to the reaction zone, leveraging their amphiphilic nature to induce structural changes in the polyamide matrix^{20–23}. This resulted in the formation of thinner films with enhanced permeability-selectivity performance, notably observed in water purification and ion separations.

However, the potential of covalently incorporating crown ethers into membranes for organic solvent filtration and pharmaceutical separations has yet to be explored. Crown ethers, with their unique cavity sizes and complexation properties, could significantly enhance the selectivity and efficiency of membranes for challenging separations such as ions, amines, and amino acids^{24–27}. Exploring this strategy could advance membrane selectivity beyond the technologies available today.

Herein, we propose and demonstrate an effective strategy to fabricate highly selective polyamide nanofilms from amino-functionalized crown ethers (Fig. 1). The fabrication procedure involves the interfacial polymerization reaction between bis(amino-benzo)-18-crown-6 (18C6) and trimesoyl chloride (TMC) on top of a

crosslinked porous support (Fig. 1). To assess the impact of the macrocycle on the separation performance, benchmark membranes are fabricated using two additional amino-functionalized polyether monomers. These monomers, consisting of ethyleneoxy repeating units with either open or distinct cyclic configurations, essentially produce polyamide active layers with similar chemical composition but lack the intrinsic porosity of the macrocycle. The separation performance is characterized by using a mixture of solutes, including active pharmaceutical ingredients (APIs) with diverse structures and chemical functionalities. Moreover, mapping the binary selectivity helps us understand the separation behavior of the membranes further beyond their molecular weight cutoff (MWCO), holding potential for advancing molecular separations in OSN and OSRO.

Results

Formation of polyamide nanofilms with crown ether moieties

The chemical structure of the polyamide nanofilms made from 18C6 was verified using FTIR (Fig. 2a and Supplementary Fig. 5). Following the interfacial polymerization reaction, the absorption bands of primary amine groups in the spectrum of 18C6 at 3356 cm⁻¹ and 3422 cm⁻¹ due to N–H symmetrical and asymmetrical stretching vibrations were reduced in the polyamide film. A broad peak in the region of 3100–3600 cm⁻¹ was also observed in the spectrum of the polyamide film, which could be assigned to residual hydroxyl groups or moisture²⁸. Moreover, a new peak appeared at 1663 cm⁻¹, which could be attributed to the carbonyl (C=O) bond stretches of the secondary amide groups. Additional less pronounced peaks appeared at 1539 cm⁻¹ and 1426 cm⁻¹, which could be due to the interactions between N–H bending and C–N stretching vibrations in the C–N–H group and C–N stretches, respectively^{28,29}. Successive peak broadening and overlapping were also observed after polymerization. This supports the formation of the polyamide film by the reaction between 18C6 and TMC. The spectrum of the film retained the characteristic peaks of the crown ether at 1231 cm⁻¹ and 1130 cm⁻¹, which could be assigned to the Ph–O–C and C–O–C bonds^{28,30}. This finding and the overall similarity between the spectra of the monomer and the network indicate the successful integration and integrity of the crown ether structure after polymerization. However, the peaks of amide I and amide II overlap with those of the crosslinked polyacrylonitrile support, especially for membranes made from polyether building blocks (Supplementary Fig. 5).

The chemical composition of polyamide nanofilms incorporating 18C6 was further studied by high-resolution XPS. The survey and high-resolution XPS spectra of the 18C6 powder and freestanding polyamide film (FS_{18C6}) were obtained and shown in Fig. 2b–e and Supplementary Fig. 6a–d. Three elements (carbon, oxygen, and nitrogen) were detected from the survey spectra of the monomer and polyamide film (Fig. 2b and Supplementary Fig. 6a). The C_{1s} core level spectrum of 18C6 monomer was fitted with five components located at 284.4, 285.1, 286.3, 289.5 eV, and 291.1 eV, which were respectively attributed to C=C, C–C, C–O/C–N, O–C=O, and π–π* shake-up satellites (Supplementary Fig. 6b)^{7,31,32}. Following the interfacial polymerization reaction, an additional component was observed in the C_{1s} spectrum of the film at 287.8 eV, which could indicate the presence of the carbonyl bond (O=C–NH) of the amide group (Fig. 2c)^{7,29,31–33}. The N_{1s} core level spectrum of the 18C6 monomer shows a dominant component located at 398.9 eV, corresponding to NH₂ (Supplementary Fig. 6c)^{7,33,34}. However, the N_{1s} core level spectrum of the film is dominated by a component located at 399.8 eV attributed to O=C–NH (Fig. 2d)^{7,33}. The contribution of the NH₂ bond was significantly lower in the N_{1s} spectrum of the polyamide film compared to the 18C6 monomer, which suggests the formation of a crosslinked polyamide network (Fig. 2d and Supplementary Fig. 6c). The interfacial polymerization reaction is further indicated by the high intensity of the carbonyl bond (O=C–NH) of the amide group in the O_{1s} spectrum of the film, which

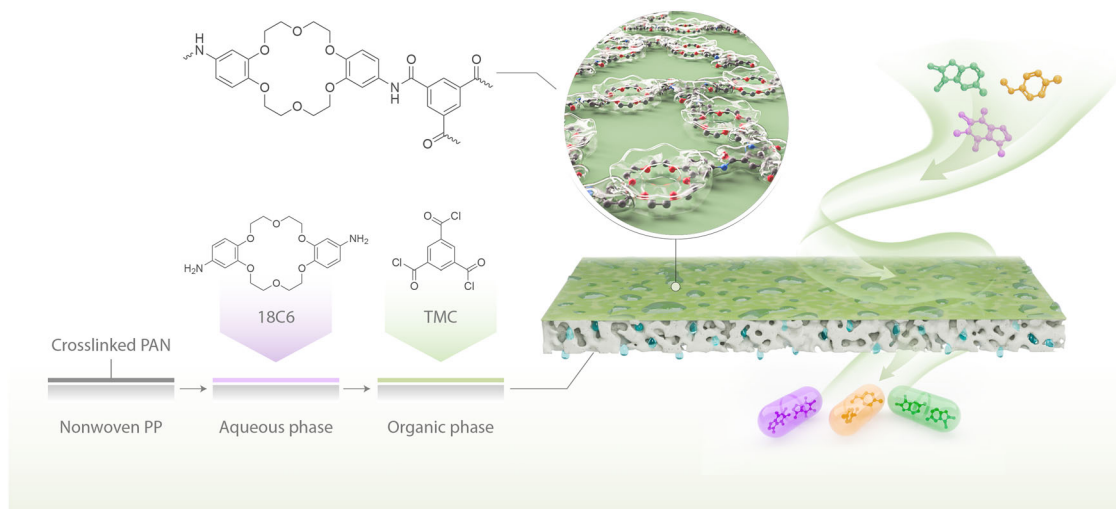


Fig. 1 | Interfacial polymerization for the fabrication of membranes. Amino-functionalized crown ether (18C6) were dissolved in the aqueous phase on a polyacrylonitrile asymmetric porous support. The support was then exposed to an organic phase with trimesoyl chloride (TMC) to react and form a thin selective layer.

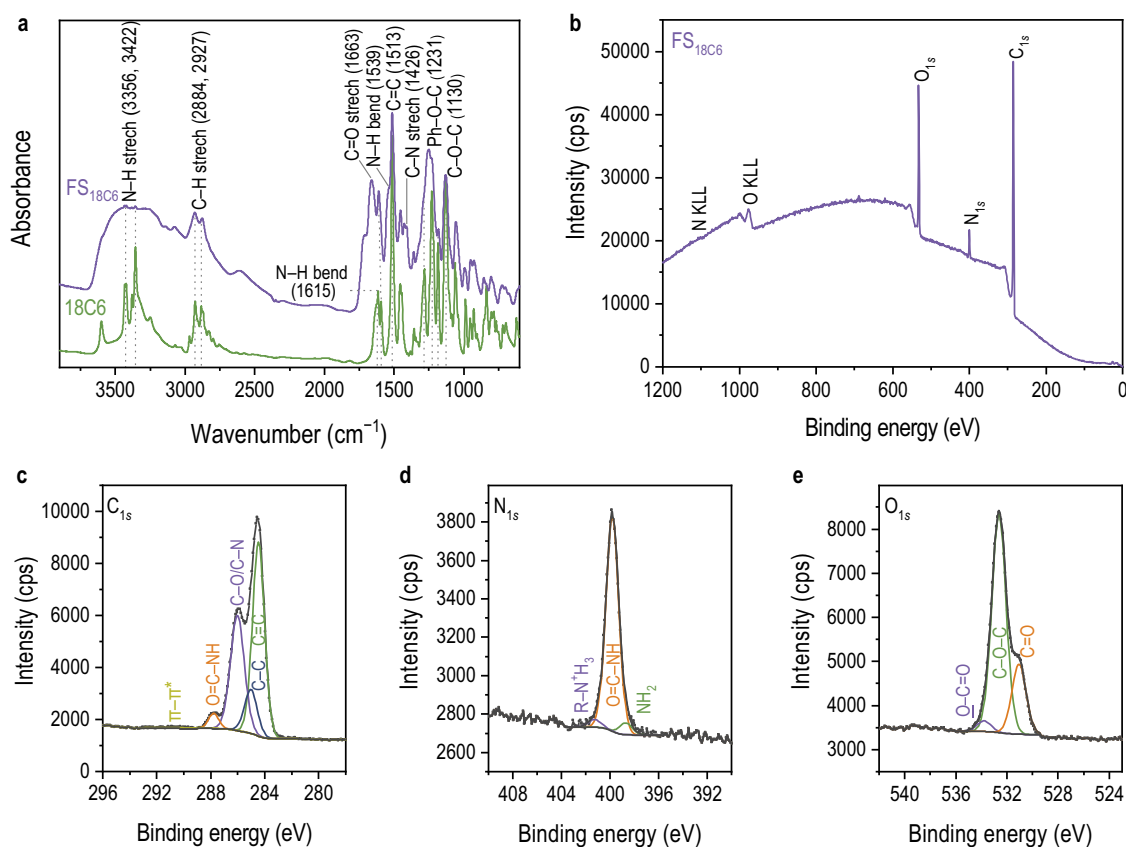


Fig. 2 | Chemical characterization of polyamide nanofilms prepared with 18C6. **a** FTIR spectra of 18C6 monomer (in green) and freestanding nanofilms (in purple) collected from the interface between the aqueous and organic phases. XPS **(b)** survey scan and **(c)** C_{1s}, **(d)** N_{1s}, and **(e)** O_{1s} core level spectra of freestanding nanofilms made from 18C6. The C_{1s} core level spectrum was fitted with five components located at 284.4, 285.0, 286.0, 287.8, and 291.1 eV, attributed to C = C, C - C,

C - O/C - N, O = C - NH and π - π^* shake-up satellites, respectively^{7,29,31–33}. The N_{1s} core level spectrum was fitted with three components located at 398.8, 399.8, and 401.6 eV attributed to NH₂, O = C - NH, and R - N⁺H₃, respectively^{7,33}. The O_{1s} core level spectrum was fitted with three components located at 531.0, 532.6, and 533.9 eV attributed to C = O, C - O - C and O - C = O, respectively^{31,33}.

was barely noticeable in the 18C6 spectrum (Fig. 2e and Supplementary Fig. 6d)^{31,33}. The component located at 532.8 eV attributed to the ether bond (C - O - C) of the crown ether was also observed in the O_{1s} spectrum of the film (Fig. 2e and Supplementary Fig. 6d)^{31,33,35,36}. These

findings confirm the formation of a crosslinked polyamide network by the reaction of 18C6 and TMC.

The scanning electron microscopy (SEM) images of the interfacially polymerized TFC membranes on top of a crosslinked

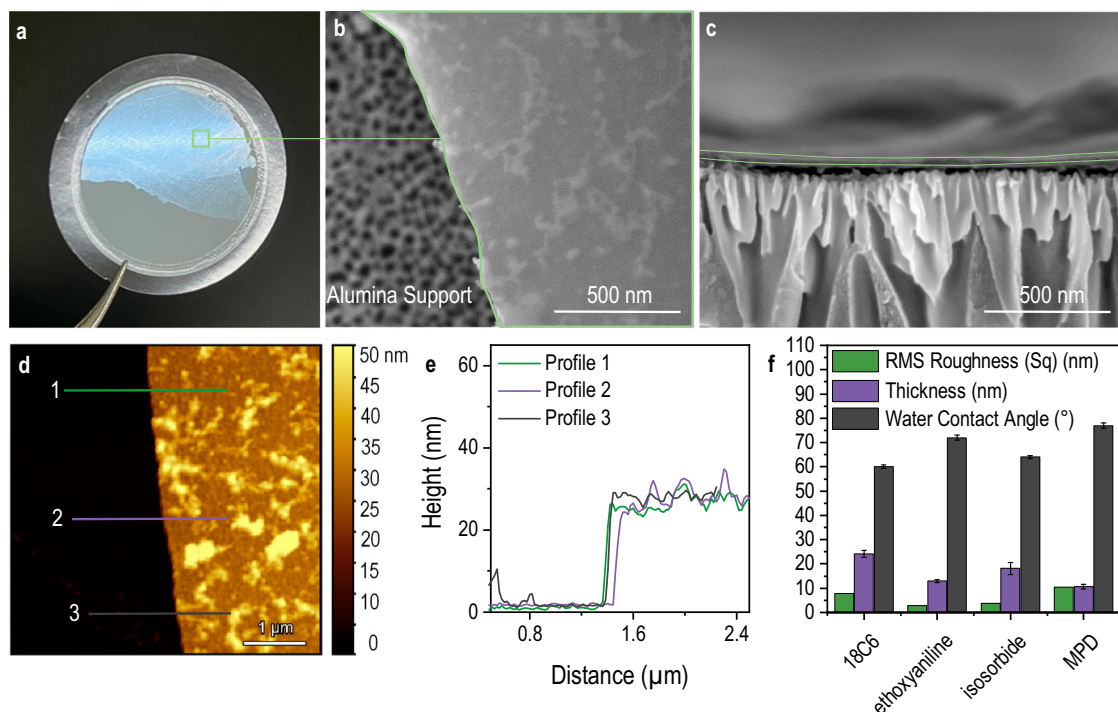


Fig. 3 | Morphology of polyamide nanofilms. **a** Photograph, **(b)** surface, and **(c)** cross-sectional SEM images of freestanding nanofilms fabricated from 18C6 on an aluminum oxide porous support. **d** AFM image and **(e)** height profile of

freestanding nanofilms prepared with 18C6 on a silicon wafer. **f** Root mean square (RMS) roughness (S_q), thickness, and water contact angle of freestanding nanofilms and TFC membranes made from different aqueous phase monomers.

polyacrylonitrile support are shown in Fig. 3 and Supplementary Fig. 7. The SEM images of membranes containing polyether building blocks showed continuous smooth surfaces that followed the topography of the polyacrylonitrile support (Supplementary Fig. 7a–d). The boundary layers between the polyacrylonitrile support and the polyamide nanofilms are hardly distinguishable in the cross-sectional SEM images (Supplementary Fig. 7f–i). Therefore, to better estimate the thickness of the polymerized layer, freestanding nanofilms were prepared under the same conditions, floated on water, and then transferred onto another substrate (Fig. 3a, b). Nanofilms prepared with 18C6 as the aqueous phase monomer had an average thickness of approximately 24 nm and a roughness of 7.9 nm, as shown in the SEM cross-sectional micrographs and atomic force microscopy (AFM) images (Fig. 3c–e and Supplementary Fig. 8a–d). By increasing the interfacial polymerization reaction time from 1 to 3 min, the nanofilm thickness slightly increased from 24 to 26 nm (Supplementary Figs. 9, 10). However, a further increase in the reaction time to 5 min had no effect on the film thickness, which suggests the formation of a dense barrier hindering monomer diffusion, a well-reported self-limiting mechanism^{37,38}. Analogous freestanding films prepared using ethoxyaniline and isosorbide as aqueous phase monomers presented similar smooth surfaces with an average thickness between 13 and 20 nm (Fig. 3f and Supplementary Fig. 8e–l). The thickness of membranes derived from polyether-based precursors observed from cross-sectional SEM micrographs is consistent with the AFM measurements (Supplementary Fig. 7g–i). Meanwhile, the benchmark free-standing MPD–TMC film fabricated at the water–hexane interface exhibited a slightly lower thickness and a higher roughness compared to other films (Fig. 3f and Supplementary Fig. 8m–p). Moreover, the surface and cross-sectional SEM micrographs retained the typical “ridge-and-valley” morphology of traditional polyamide composite membranes with an average thickness of approximately 100 nm (Supplementary Fig. 7e, i). Herein, rationalizing the thickness and roughness behaviors between the different interfacial polymerization

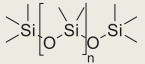
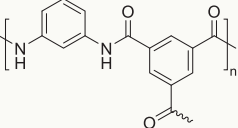
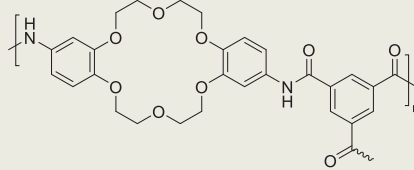
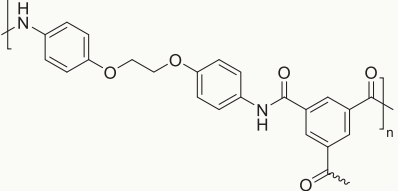
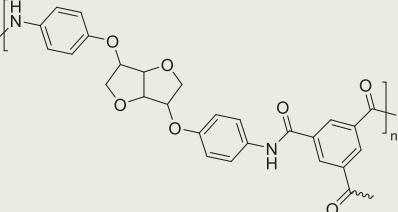
systems relies heavily on the differences in reactivity and diffusivity between the monomers utilized in the aqueous phase. The low roughness observed for membranes derived from polyether-based precursors can be explained by the low diffusivity of the relatively large monomers compared to classical diamines, most notably MPD (Supplementary Fig. 7b–e)^{14,39}. The addition of a co-solvent to enhance the solubility of the polyether-based monomers could also influence the reaction zone by reducing the interfacial tension with the organic phase and increasing the solubility of TMC in the aqueous phase, hence yielding a higher thickness⁴⁰.

The hydrophilicity of the membranes was confirmed by the water contact angle measurements (Fig. 3f and Supplementary Fig. 7k–o). The polyacrylonitrile support had a low water contact angle of approx. 40° (Supplementary Fig. 7k), and the water droplets gradually dissipated into the porous structure. Following the surface modification, the water contact angle increased to approx. 60° for membranes prepared from crown ether, but they are still considered hydrophilic. The slight increase in contact angle can be attributed to the chemical structure of the crown ether, which contains polarized oxygen atoms and non-polar phenyl groups. Membranes prepared with ethoxyaniline and isosorbide also have ultrathin and smooth selective layers (Fig. 3f). The hydrophilicity of the surface further decreased when ethoxyaniline and isosorbide were used as the aqueous phase monomers instead of crown ether. Overall, the hydrophilicity of the membranes that contain polyether units was higher than the control membrane, which is reflected by the greater transport of polar solvents.

Molecular sieving performance

To investigate the impact of the macrocycle on the performance of the membranes, we assessed membranes composed of analogous polyether-based monomers (ethoxyaniline and isosorbide) and compared them with the polyamide membrane containing crown ether (Table 1). The monomers consist of ethyleneoxy repeating units with either open or distinct cyclic configurations. This leads to the

Table 1 | The structure and properties of the membranes investigated in this work

Membrane	Interfacial Polymerization System	Active Layer Chemical Structure
DuraMem®150	NA	Crosslinked polyimide
GMT-oNF-2	NA	
TFC _{MPD}	188.7 mM MPD in water 2.5 mM TMC in hexane	
TFC _{18C6}	20.5 mM 18C6 in TFE/water (1.0 v./v.) 2.5 mM TMC in hexane	
TFC _{ethoxyaniline}	20.5 mM ethoxyaniline in DMAc/water (2.3 v./v.) 2.5 mM TMC in hexane	
TFC _{isosorbide}	20.5 mM isosorbide in DMAc/water (3.0 v./v.) 2.5 mM TMC in hexane	

formation of polyamide active layers with essentially equivalent chemical composition but lacking the intrinsic porosity provided by the macrocycle. The performance of classical polyamide TFC and commercial OSN membranes, DuraMem®150 and GMT-oNF-2, was also evaluated under the same conditions for cross-comparisons (Table 1).

The effect of using a crown ether monomer unit as a building block for polyamide film on solvent permeance is shown in Fig. 4a and Supplementary Fig. 10. The acetonitrile permeance of membranes made from the macrocycle was substantially higher than that of those prepared with ethoxyaniline and isosorbide. Specifically, the permeance of acetonitrile was as high as $7.2 \pm 0.7 \text{ L m}^{-2} \text{ h}^{-1} \text{ bar}^{-1}$, which is 95% higher than the membranes prepared with isosorbide ($0.4 \pm 0.1 \text{ L m}^{-2} \text{ h}^{-1} \text{ bar}^{-1}$) (Fig. 4a). The acetonitrile permeance of polyamide membranes prepared with polyether-based monomers of different structures does not follow a direct correlation with the surface hydrophilicity or the thickness of the films, as shown in Supplementary Table 2. This could be an indication of the higher free volume provided by the macrocycle structure and the amphiphilic nature and cavity of the crown ether, which modify the nanostructure of the polyamide film and provide pathways for increased solvent transport. The permeance of TFC_{18C6} for acetonitrile is also much higher than that of the traditional polyamide and other commercial OSN membranes, as shown in Fig. 4a. Furthermore, the permeance of acetonitrile

and methanol through the crown ether-based membrane decreased with an increase in the reaction time from 1 to 3 min (Supplementary Fig. 10). A further increase in the reaction time had no effect on the solvent permeance. This decrease in solvent permeance is correlated with the increase in the active layer thickness.

To further evaluate the potential of crown ether-based TFC membranes for OSN applications, the permeance of solvents with different properties was measured (Fig. 4b). The plot of permeance as a function of inverse viscosity did not follow a simple linear correlation, indicating that the Hagen-Poiseuille for flow under pressure without a particular interaction with the membrane (Supplementary Fig. 11). However, the solvent permeation rate through the membrane has a practically linear correlation with the combination of three solvent properties: the polar contribution to the Hansen solubility parameters (δ_p), inverse viscosity (η) and inverse molar diameter (d_m)⁷. Acetonitrile, which has the highest δ_p value ($18 \text{ MPa}^{1/2}$) and the lowest viscosity (0.32 cP), has the highest permeance, although its molar diameter (0.55 nm) is in the middle range. The permeance of polar protic solvents such as water and alcohol (methanol and ethanol) decreased with the increase in viscosity and molar diameter of the solvent. Nonpolar solvents such as toluene and heptane had the lowest permeance values. They have the lowest δ_p values and the highest molar volume. This confirms that the crown ether-based TFC

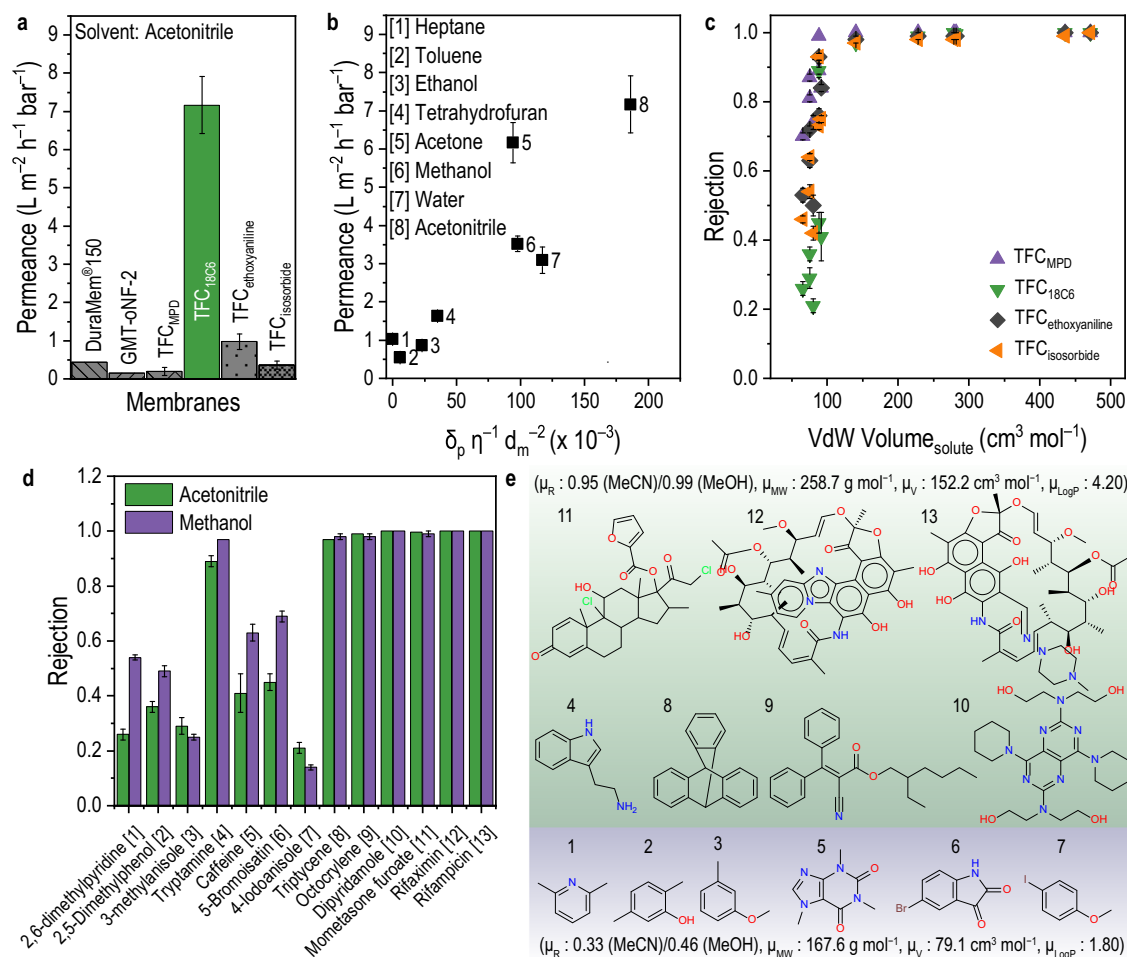


Fig. 4 | OSN and OSRO performance of TFC membranes. **a** Acetonitrile permeance through OSN commercial membranes and polyamide TFC membranes in this work. **b** Solvent permeance as a function of the combined solvent properties of the membrane prepared with 18C6. **c** Polyamide membranes rejection for structurally diverse solutes in acetonitrile as a function of their corresponding Van der Waals volumes. **d** The rejection of the solutes in acetonitrile (MeCN) and methanol

(MeOH) for the membrane prepared with 18C6. **e** Classification of the solutes according to the measured rejection values by the membrane prepared with 18C6. μ_R , μ_{MW} , μ_V , and μ_{LogP} denote the average values of rejection, molecular weight, molar volume, and partition coefficient between the organic and aqueous phases of the solutes displayed in that row.

membranes favor the transport of polar solvents with low viscosity and a small molar diameter. Acetone is the solvent with the highest deviation from the linear correlation, exhibiting the second highest permeance, although both the δ_p and d_m values are in the middle range. Acetone is the solvent with the lowest viscosity, and this is probably the predominant factor. Acetone molecules also have strong dipole-dipole interactions with each other through the keto groups, which might play a role in the transport not as single molecules but as dimers or interconnected clusters. Water also has a small deviation from the linearity in Fig. 4b. In a recent report, Elimelech's group analyzed the models available for water transport in reverse osmosis membranes and highlighted the solution-friction model's superiority over solution-diffusion^{41,42}. According to the model, the solvent permeance is inversely proportional to the friction coefficient between the permeant and the membrane pore. Water molecules permeate as clusters, being cohesively interconnected by hydrogen bonds when traveling through the networks of pores in the membrane. Overall, the permeance of different organic solvents through the membrane containing 18C6 is higher than that of DuraMem®150 and follows an opposite trend compared to GMT-oNF-2, a polydimethylsiloxane-based membrane, which shows preferential transport for non-polar solvents (Supplementary Table 3). The solvent transport through the crown ether-based membranes follows a similar trend as previously

reported macrocycle-based membranes, with some exceptions for trialemine, which has excellent transport for both polar and non-polar solvents.

The performance evaluation of membranes for OSN and OSRO is commonly conducted with simple feed solutions containing dyes, polyether, and polystyrene oligomers. However, when targeting applications in the pharmaceutical industry, membranes are used for the separation of complex mixtures of small molecules in different solvents. In this work, a mixture of 13 solutes with molecular weights below 850 g mol^{-1} (Supplementary Table 2) was used as the test feed, and the component rejection by the membranes was analyzed by HPLC. Plots of rejection as a function of Van der Waals volumes and of molecular weights are respectively shown in Supplementary Figs. 12, 13, and Fig. 4c. The correlation for all membranes, except GMT-oNF-2, was better with the Van der Waals volumes, with a clear improvement seen for molecules containing heavier elements like iodine and bromine.

All solutes with volumes in the range of $140\text{--}471 \text{ cm}^3 \text{mol}^{-1}$ ($254\text{--}823 \text{ g mol}^{-1}$) were rejected by the membranes derived from polyether-based building blocks at a rate exceeding 90%, indicating a simple size exclusion (Fig. 4c). Their estimated average pore size was similar, with the largest observed for the macrocycle-based membrane at approximately 0.34 nm (Supplementary Fig. 15). Notably, the

membranes prepared with crown ether exhibited a particularly sharp rejection profile. Solutes with volumes smaller than $100 \text{ cm}^3 \text{ mol}^{-1}$ had a more complex rejection behavior in both acetonitrile and methanol, with higher rejection rates in methanol (Fig. 4d). This observation can be attributed to the differing hydrogen binding capacity (δ_{H}) and polarity (δ_{P}) of the solvents, with methanol and acetonitrile having δ_{H} values of 22.3 and 6.1, respectively. Previous studies have also shown that the contribution of the solute properties to the rejection behavior increases with the δ_{H} and δ_{P} of the solvent, as observed for PDMS-based membranes⁴³. Therefore, the potential contribution of chemical functionalities to rejection profiles is discussed in greater detail.

A visual representation of the solutes according to their measured rejection by the crown ether-based TFC membrane is provided in Fig. 4e. LogP defines the partition coefficient between the organic and aqueous phases; polar solutes have a low or negative LogP, while solutes of low polarity have a high LogP. Aromatic hydrophobic compounds with an average LogP value of 4.2 dominated the high rejection domain. Interestingly, tryptamine ($\log P = 1.6$) exhibited an exceptionally high rejection value despite its hydrophilicity and relatively small size. This anomaly may result from complex interactions between tryptamine, the solvent, and other solutes in the system. These interactions were validated by measuring the rejection of tryptamine and rifampicin as a single solute in acetonitrile (Supplementary Fig. 12). The rejection of rifampicin by TFC_{18C6} is the same as a single solute or in a mixture; however, a negative value was obtained for tryptamine as a single solute. This may suggest the formation of clusters due to the interactions between the solutes, thereby increasing the observed rejection⁴⁴. Solute rejection values lower than 0.5 were predominantly hydrophilic fine chemicals with an average LogP of 1.8. The stability of the membranes prepared with 18C6 was assessed over four days using a mixture of 13 solutes in methanol. As shown in Fig. 16, no significant fluctuations in flux or rejection were observed. Moreover, the flux and rejection of solutes were found to be linearly proportional to the applied pressure gradient, indicating that the nanostructure of the active layer remained stable (Supplementary Fig. 17).

The rejection behavior of thirteen solutes in acetonitrile by GMT-oNF-2 did not follow a clear correlation with size in the range of $88\text{--}228 \text{ cm}^3 \text{ mol}^{-1}$ (Supplementary Fig. 12e). To comprehend the transport mechanism of these solutes, we examined the Hansen solubility parameters (HSPs) to estimate the extent of interactions between the polymer membrane, the solutes, and the solvent. Zeidler et al.⁴⁵ reported that the closer the solubility parameters of polysiloxane-based membranes and the solvent are, the higher the solvent flux. The separation behavior of solutes containing the same core structure with different functional groups revealed that high rejection values were attained when the affinity of the solutes to the solvent was very high relative to their interactions with the membrane. When the solubility parameters indicated that the solute had a high affinity for the membrane, dissolution of the solutes in the membrane materials was favored, and low rejection was observed⁴⁵. As shown in Supplementary Table 6, we determined the distance between the solubility parameters (R_{A}^2) of the polysiloxane active layer, acetonitrile, and the solutes. The results indicated a low affinity between the membrane and acetonitrile; as a consequence, the permeance was relatively low. When the solutes had a higher affinity for the membrane than the solvent, as in solutes 1, 2, 3, 7, and 9, the rejection became negative. The rejection increased as the solubility parameter of the solute approximated that of the solvent. Therefore, for elastomeric membrane selective layers like GMT-oNF-2, molecular size is not the only factor affecting selectivity. The interaction between solute and membrane becomes relevant. This behavior has some correlation with what is observed for gas and vapor separation in polymeric membranes. The separation of gas and vapors in membranes constituted by

glassy rigid polymers is predominantly based on differences in diffusivity and, therefore, on the available free volume. In elastomeric membranes like those based on polydimethylsiloxane, solubility plays a more important role.

Advancing molecular selectivity

The membranes demonstrated in this work have a high-performance with high rejection of molecules with Van der Waals volume above $100 \text{ cm}^3 \text{ mol}^{-1}$ and acetonitrile permeance above $7 \text{ L m}^{-2} \text{ h}^{-1} \text{ bar}^{-1}$. However, what distinguishes the crown ether membranes from commercial ones and from others prepared in the lab with analogous chemistry without the macrocyclic structures is their efficiency in separating pairs of solute molecules with molecular weights below 800 g mol^{-1} . To assess the separation performance of the membranes, the selectivity figure of merit ($\text{SFM}(\beta_{\text{A/B}})$) was calculated for all possible solute pairs. We present the values for the TFC membrane made from amino-functionalized crown ether in the matrix shown in Fig. 5a. Supplementary Table 7 extends the data for all membrane types. In general, we observed that the binary selectivity increases as the size difference between the solutes increases (Fig. 5a). We identified high separation factors between APIs with molecular weights around 800 g mol^{-1} , Rifaximin (12) or Rifampicin (13), and small organic molecules. This suggests that TFC_{18C6} is an excellent membrane for purifying these APIs from smaller impurities. However, the separation is more challenging for fine solutes with similar kinetic diameters. We found that TFC membranes prepared with crown ether are suitable for separating solute pairs with molecular weights between 100 and 370 g mol^{-1} (Fig. 5b). For example, the normalized separation factors between 4-iodoanisole (234 g mol^{-1}) and triptycene (254 g mol^{-1}) or octocrylene (361 g mol^{-1}) were 28.6 and 49.3, respectively. Notably, the difference in polarity between these solutes could significantly contribute to their high separation factors. In addition, the incorporation of the macrocyclic crown ether into polyamide films had a positive effect on both permeance and average SFM when compared to benchmark membranes tested under the same conditions (Fig. 5c). The comparison of the performance of the crown ether-based membrane to membranes reported in the literature revealed superior selectivity for solutes in the molecular weight range $200\text{--}500 \text{ g mol}^{-1}$ (Supplementary Fig. 18 and Supplementary Table 8).

Furthermore, the observed correlation between rejection selectivity ($\beta_{\text{A/B}}$) and the rejection of the less permeable solute (R_{B}) allows us to compare the separation performance of different membranes (Fig. 6). As reported in our prior work, the rejection selectivity data is distributed along a diagonal grid that decreased as $\log(1-R_{\text{B}})$ increased⁴⁶. The broader the distribution of points in the x - y plane, the better the changes to separate solutes of similar characteristics and the larger the overall rejection selectivity of the membrane. In other words, the larger the area covered by the measured points, the higher the overall rejection selectivity. Therefore, although the DuraMem®150 membranes can reject small solutes with Van der Waals volumes around $100 \text{ cm}^3 \text{ mol}^{-1}$ and would be useful for the concentration of a complex mixture of solutes, they could not fractionate them or separate pairs of small molecules. On the other hand, the TFC membrane prepared with crown ether is the one with the maximal distribution. The performance of TFC_{18C6} compared to the other membranes highlights the potential for fine-tuning the selectivity at the molecular level. By tailoring membrane selectivity toward solutes with similar physicochemical properties, we can open avenues for customizing membranes for specific applications.

Discussion

We propose an effective strategy for fabricating and evaluating highly selective polyamide nanofilms tailored for the concentration and

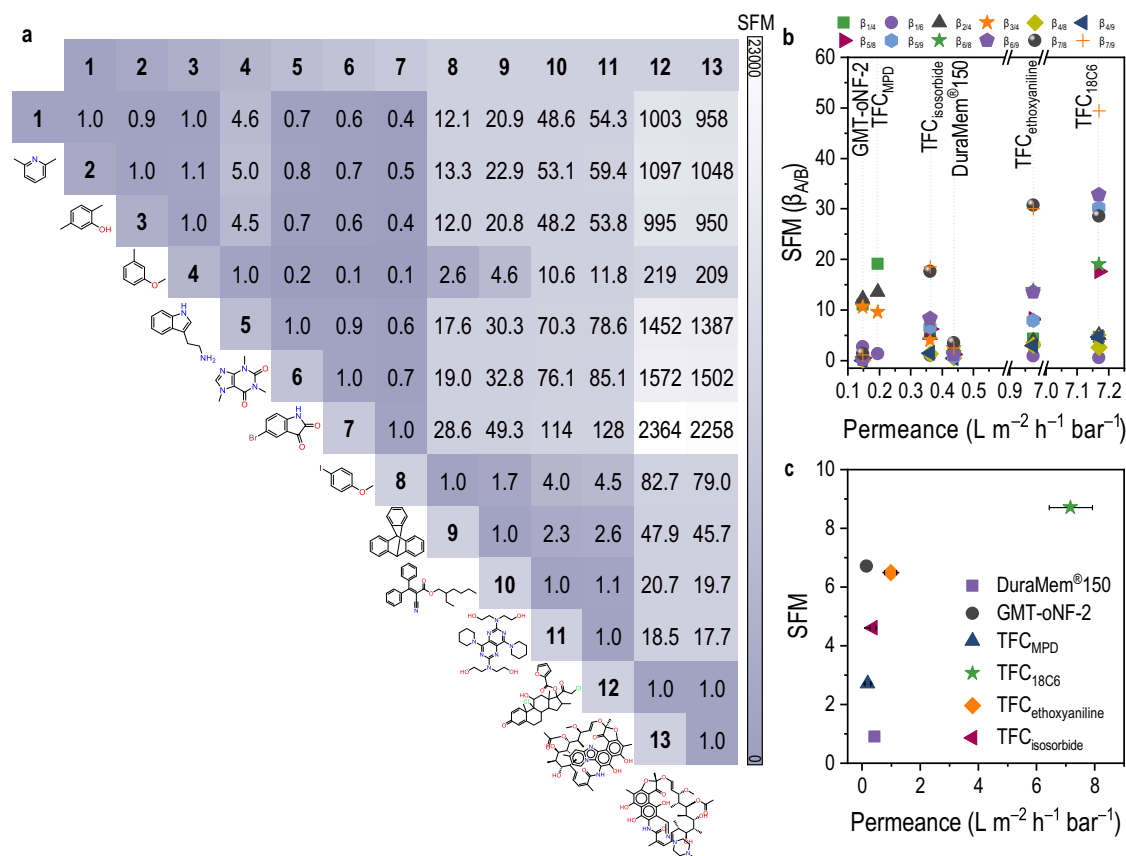


Fig. 5 | Binary selectivity for polyamide TFC in this work and benchmark membranes. **a** The selectivity figure of merit (SFM ($\beta_{A/B}$)) matrix for TFC_{18C6} with all possible binary combinations. **b** Trade-off between acetonitrile permeance and

SFM ($\beta_{A/B}$) for solute pairs of similar size. **c** Trade-off between acetonitrile permeance and average SFM values. The average values exclude markers with a rejection value of 1.0.

separation of complex mixtures or solutes. The successful synthesis of nanofilms utilizing amino-functionalized crown ether building blocks through interfacial polymerization has produced ultrathin active layers measuring ~20 nm in thickness. Comparative analysis with benchmark membranes (Supplementary Fig. 13 and Supplementary Table 6)^{2,7,8,14,15,18,47}, incorporating polyether-based monomers (ethoxyaniline and isosorbide) with different open and cyclic configurations, underscores the unique performance attributed to the distinctive macrocyclic structure of the crown ether. Notably, the acetonitrile permeance of membranes incorporating crown ether exhibited a remarkable 93% increase compared to benchmark and commercial OSN membranes. This enhancement could be attributed to the macrocycle, which leads to the formation of polyamide nanofilms with pathways for increased solvent transport. Furthermore, crown ether-based membranes outperformed commercially available nanofiltration membranes by 23–90% selectivity margins. Mapping the selectivity with a mixture of structurally diverse solutes revealed effective rejection of active pharmaceutical ingredients with molecular weights around 800 g mol⁻¹. This characteristic would enable the effective concentration of molecules in this size range or their separation from smaller ones. Our research also demonstrates the efficacy of TFC membranes incorporating crown ether in separating solute pairs with molecular weights ranging from 100 to 370 g mol⁻¹. The notable separation factors observed for specific solute pairs, such as 4-iodoanisole and triptycene or octocrylene, enable the application of these membranes for precise molecular separations via OSN and OSRO. Overall, this research not only contributes to the development of advanced membrane materials with enhanced selectivity but also holds promise for addressing complex separation challenges in the pharmaceutical and chemical industries.

Methods

Materials

Polyacrylonitrile porous flat-sheet membranes cast on polypropylene nonwoven support were purchased from GMT Membrantechnik GmbH, Germany. Two commercial OSN membranes, GMT-oNF-2 and DuraMem® 150, were respectively supplied by GMT Membrantechnik GmbH and Evonik. GMT-oNF-2 is a TFC membrane with an apolar rubbery polydimethylsiloxane-based active layer and a reported RWCO of 350 g mol⁻¹. DuraMem®150 is a crosslinked polyimide with a lower reported MWCO of 150 g mol⁻¹. 4,4'-(Ethane-1,2-diylbis(oxy)) dianiline (ethoxyaniline) (99%) and 4,4'-(diamino)-1,4:3,6-dianhydro-2,5-di-O-phenyl-D-sorbitol (isosorbide) (>98%) were purchased from Luminescence Technology Corporation. Hydrazine monohydrate (98%), trimesoyl chloride (TMC) (>98%), *m*-phenylene diamine (MPD) (99%), and sodium metabisulfite (97%) were all purchased from Sigma Aldrich. *n*-Hexane (97%), *N,N*-dimethylacetamide (DMAc) (>99.9%), 2,2,2-trifluoroethanol (TFE) (98.8%), and HPLC-grade acetonitrile were purchased from VWR. Deionized (DI) water used in all experiments was filtered through a Millipore Milli-Q water purification system.

Synthesis of bis(aminobenzo)-18-crown-6 (18C6)

The monomer, bis(aminobenzo)-18-crown-6 (18C6), was synthesized according to the following procedure (Supplementary Fig. 1). Dibenzo-18-crown-6 (I) (20 g, 1 eq, 55 mmol) was dissolved in chloroform (104 mL). Acetic acid (78 mL) was added to the solution over 10 min, which was then stirred at room temperature for an additional 5 min. A solution of nitric acid (II) (6.3 g, 4.5 mL, 1.8 eq, 0.10 mol) in acetic acid (10 mL) was added dropwise over 15–20 min. The solution was stirred at room temperature for 1 h and then heated to reflux overnight, whereupon a precipitate formed. The solution was allowed to cool to

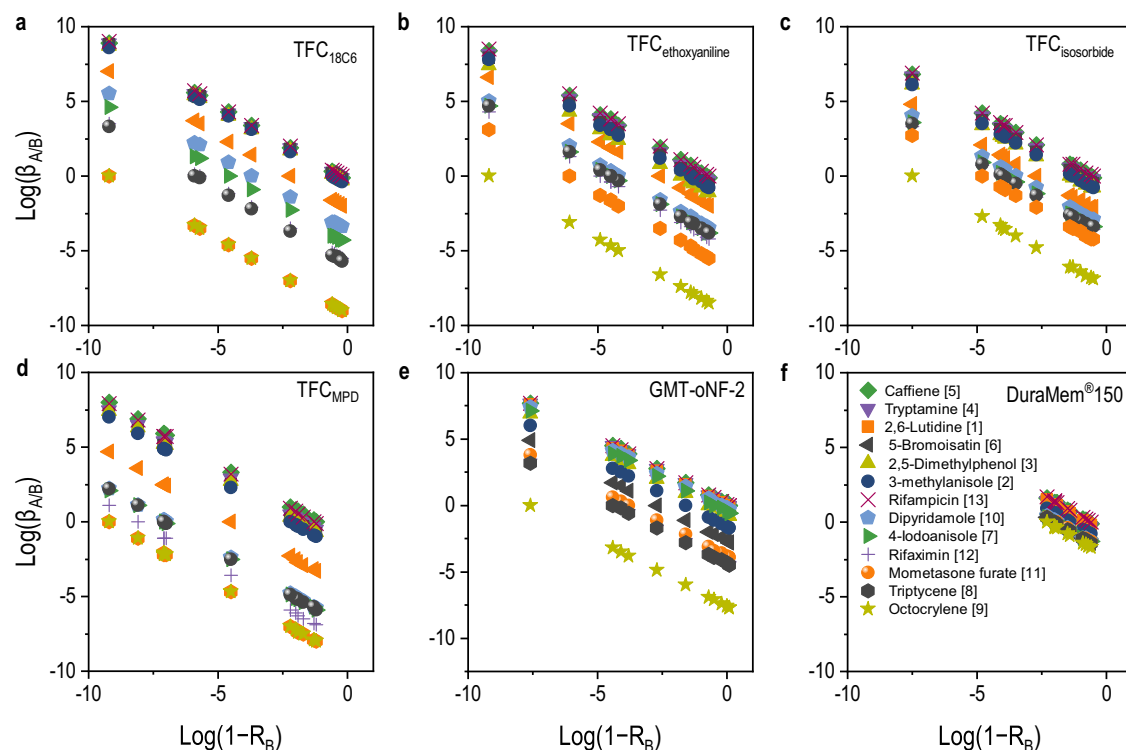


Fig. 6 | Distribution of rejection selectivity as a function of $\log(1 - R_B)$ for all possible solute pairs tested with different membranes. a TFC_{18C6}, **(b)** TFC_{ethoxyaniline}, **(c)** TFC_{isosorbide}, **(d)** TFC_{MPD}, **(e)** GMT-oNF-2, and **(f)** DuraMem®150.

room temperature. After 48 h, the precipitation was filtered, and the compound was isolated as a pale yellow solid. Residual acetic acid was removed by dissolving the sample in dimethylformamide (DMF), followed by the addition of water to precipitate pure bis(nitrobenzo)-18-crown-6 (III) (2.7 g, 6.0 mmol, 11%). Supplementary Fig. 2 shows the ^1H NMR and ^{13}C NMR for bis(nitrobenzo)-18-crown-6 in deuterated dimethyl sulfoxide (DMSO- d_6). ^1H NMR (400 MHz, DMSO- d_6) δ 3.85 (m, 8H), 4.21 (m, 8H), 7.15 (d, 2H, $J = 9$ Hz), 7.72 (d, 2H, $J = 2.7$ Hz), 7.89 (dd, 2H, $J = 9, 2.7$ Hz). ^{13}C NMR (75 MHz, DMSO- d_6) δ 153.8, 147.7, 140.6, 117.6, 111.3, 106.6, 68.4, 68.0.

Subsequently, the intermediate product (III) (20 g, 1 eq, 44 mmol) was suspended in ethanol (800 mL), and hydrazine (IV) (14 g, 14 mL, 10 eq, 0.44 mol) was added. After 10 minutes of stirring, the reaction mixture was heated to reflux. After 30 minutes, the reaction mixture was filtered while hot, then cooled, and the product crystallized as a white compound. The product was purified by recrystallization from ethanol. Supplementary Fig. 3 shows the ^1H NMR and ^{13}C NMR for 18C6. ^1H NMR (400 MHz, DMSO) δ 6.63 (d, $J = 8.5$ Hz, 1H), 6.27–6.22 (m, 1H), 6.06 (dd, $J = 8.5, 2.4$ Hz, 1H), 3.95 (dtd, $J = 17.4, 5.7, 3.0$ Hz, 4H), 3.79 (dq, $J = 18.1, 5.0$ Hz, 5H). ^{13}C NMR (101 MHz, DMSO) δ 149.64, 149.53, 143.94, 143.87, 139.61, 139.53, 116.05, 115.86, 105.72, 101.17, 101.09, 69.87, 69.71, 69.65, 69.52, 68.13, 68.04.

Crosslinking of the polyacrylonitrile porous support

The polyacrylonitrile support was crosslinked according to a previously published protocol⁴⁸. To enhance its chemical stability, the support was crosslinked at 85 °C for 6 h in 20% (v/v) hydrazine hydrate in DI water. The crosslinked membranes were washed and stored in DI water to remove the excess crosslinker and maintain their wettability.

Solubility of 18C6 and analogous ethyleneoxy-based monomers

The ethyleneoxy-based monomers, shown in Table 2, have poor solubility in water at neutral pH. Therefore, the monomers were dissolved in a co-solvent system containing different volume ratios of an

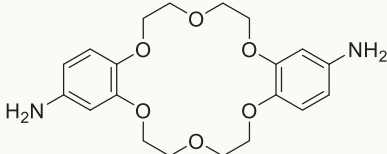
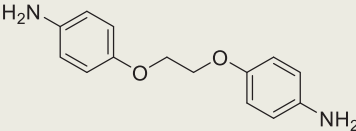
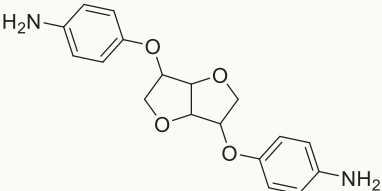
organic solvent to water. Initial solubility studies revealed that all three monomers are soluble in polar aprotic solvents such as dimethyl sulfoxide (DMSO), *N,N*-dimethylacetamide (DMAc), and *N,N*-dimethylformamide (DMF). 18C6 and ethoxyaniline are also soluble in fluorinated alcohols such as 2,2,2-trifluoroethanol (TFE). The volume ratio of the organic solvent to water was determined at a fixed concentration of 20.5 mM for each monomer. The monomers were first dissolved in the organic solvents and sonicated for 2 min. Then, water was slowly added and sonicated for another 10 min. These aqueous solutions were then filtered through a 0.20 μm syringe filter and used to prepare thin-film composite membranes on top of crosslinked polyacrylonitrile supports.

Interfacial polymerization

The interfacial polymerization method was used to make polyamide composite membranes (Fig. 1). In this method, an amine monomer and an acyl chloride monomer are dissolved in immiscible solvents, and at their interface, the polymerization takes place, forming a thin film on top of a microporous support. The wet, crosslinked polyacrylonitrile support was allowed to dry at room temperature for 30 min. The pristine support was mounted on a Teflon plate and frame set-up and impregnated with 10 mL of 20.5 mM 18C6 aqueous solution for 1 min (Table 2). After removing the excess solution with a custom-made air knife, the membrane's surface was exposed to 10 mL of 2.5 mM (0.1 wt.%) TMC in hexane for 1 min. The membrane was afterward washed with 10 mL of hexane, heat treated at 80 °C for 5 min, washed with DI water, and then stored in a 1000 ppm sodium aqueous metabisulfite solution at 4 °C. The support impregnation and interfacial polymerization reaction were carried out at room temperature.

Control membranes were fabricated following the same method, but the aqueous phase monomer was replaced by either 20.5 mM ethoxyaniline or 20.5 mM isosorbide (Table 2). Classical polyamide membranes were also prepared from 188.7 mM (2 wt.%) MPD in water as the aqueous phase solution.

Table 2 | Chemical properties and solubility of 18C6 and analogous ethyleneoxy-based monomers

Monomer	Chemical structure	MW (g mol ⁻¹)	Aqueous Solvent (v./v.)
18C6		390	TFE/water (1.0)
Ethoxyaniline		244	DMAc/water (2.3)
Isosorbide		328	DMAc/water (3.0)

Fabrication of freestanding films

Freestanding films were collected from the aqueous-organic interface, as shown in Supplementary Fig. 4. 10 mL of aqueous and organic phase solutions were added to a glass Petri dish and allowed to react for 1 min. The films were afterward collected from the interface on a substrate, rinsed with hexane to remove residual acyl chloride, floated on the water, and picked up on either a silicon wafer, a gold-coated silicon wafer, or an aluminum oxide anodisc filter (pore size 0.02 μm). A 24 h reaction time was carried out for samples used for Fourier Transform Infrared (FTIR) measurements. The films were collected from the interface, washed with hexane and water, and then dried overnight at 80 °C.

Characterization methods

The liquid phase nuclear magnetic resonance (NMR) measurements were recorded on a Bruker Avance III operating at a 400 MHz resonance frequency. Fourier Transform Infrared (FTIR) spectra were acquired using a Nicolet iS10 spectrometer (Thermo Fisher Scientific) for wavenumbers between 4000–400 cm⁻¹. The FTIR spectra for the TFC membranes were obtained in attenuated total reflectance (ATR) mode with 16 scans and a resolution of 4 cm⁻¹. The FTIR spectra for the powder samples were acquired in transmission mode on potassium bromide pellets (0.7 wt.%) with 16 scans and a resolution of 4 cm⁻¹. X-ray photoelectron spectroscopy (XPS) studies were carried out in a Kratos Axis Supra DLD spectrometer equipped with a monochromatic Al Kα X-ray source (hν = 1486.6 eV) operating at 150 W, a multi-channel plate, and a delay line detector under a vacuum of ~10⁻⁹ mbar. All spectra were recorded using an aperture slot of 300 μm × 700 μm. Survey spectra were collected using a pass energy of 160 eV and a step size of 1 eV. A pass energy of 20 eV and a step size of 0.1 eV were used for the high-resolution spectra. Scanning electron microscopy (SEM) images were acquired on a Magellan field-emission scanning electron microscope with an accelerating voltage of 3 kV and a working distance of 4 mm. The membranes were cut and mounted on an aluminum stub using conductive aluminum tape. The cross-section samples were fractured in liquid nitrogen. To avoid surface charging, a 6 nm thick coating of iridium was sputter-coated using Quorum Technologies Q150T under an argon atmosphere. Atomic force microscopy (AFM)

images were obtained on a Dimension ICON scanning probe microscope under tapping mode in air to analyze the 3D morphologies and roughness of the membranes. The root mean square roughness (RMS) was calculated for the height profile of each 5 μm × 5 μm sample. To study the surface-wetting nature of the membranes, water contact angles were evaluated via the sessile drop method on the FM40 Easy Drop instrument (KRÜSS) at room temperature. A 2-μL water droplet was carefully placed on the membrane using a microsyringe. The reported contact angle values are the averages of three measurements.

Membrane performance

The organic solvent nanofiltration experiments were carried out using a 4-way dead-end stainless-steel cell (Textop Ltd., Hungary) at room temperature and a constant stirring speed of 150 rpm. The feed chamber was pressurized using nitrogen gas. Two membrane samples with an effective area of 4.9 cm² were loaded into the cell and tested in parallel using a feed volume of 400 mL. The membranes were initially compacted at 25 bar or 35 bar for one hour. The transmembrane pressure was afterward reduced to 20 or 30 bar, and the steady-state flux of pure solvents was determined by measuring the volume (*V*) per unit area (*A*) per unit time (*t*) according to Eq. (1).

$$J = \frac{\Delta V}{A \cdot \Delta t} \left[\frac{\text{L}}{\text{m}^2 \text{h}} \right] \quad (1)$$

The permeance was calculated according to Eq. (2).

$$P = \frac{\Delta V}{A \cdot \Delta t \cdot p} \left[\frac{\text{L}}{\text{m}^2 \cdot \text{h} \cdot \text{bar}} \right] \quad (2)$$

where *p* is the transmembrane pressure.

The permeance of different solvents was measured in the following sequence: methanol, ethanol, acetonitrile, acetone, tetrahydrofuran, heptane, and toluene. The properties of the solvents are summarized in Supplementary Table 1. The solute rejection was evaluated using a mixture of solutes with the properties shown in Supplementary Table 2. The mixture was prepared in acetonitrile at a fixed concentration of 0.25 mM of each solute. A 400 mL of the mixture was

used as feed; the first 10 mL was discarded, and three permeate samples of 1.5 mL were collected. The samples were analyzed using a high-performance liquid chromatography (HPLC) system (Ultimate 3000, Thermo Scientific) equipped with a UV detector (Diode Array Detector, Thermo Scientific). The column was a Hypersil GOLD, 100 × 2.1 mm, 1.9 μm (Thermo Scientific), using 0.1 wt.% ammonium acetate in LCMS-grade water (A) and HPLC-grade acetonitrile (B) as the mobile phase. The total run time for each injection was 42 min with a 3-μL injection volume. The selected wavelength included the highest absorption wavelength for each solute, namely 220, 254, 272, 320, 215, 232, and 262 nm. The column oven temperature was maintained at 45 °C, the vaporizer temperature of the ISQEM was set to 200 °C, and the ion transfer tube temperature was 300 °C. A hybrid isocratic gradient elution with a flowrate of 0.5 mL min⁻¹ was used for the measurements. The data was manually integrated into Chromeleon 7. At least two samples of each membrane type were tested to ensure the reproducibility of the results.

The concentrations of the feed (C_F), permeate (C_P), and retentate (C_R) were estimated based on the area under the curve (AUC) for each chemical and used to determine the rejection (R) values as follows:

$$R = 1 - \frac{C_P}{C_R} = 1 - \frac{AUC_P}{AUC_R} \quad (3)$$

The separation factor for compound A over compound B was calculated using the following equation:

$$\beta_{A/B} = \frac{C_P^A}{C_F^A} \cdot \frac{C_F^B}{C_P^B} = \frac{1 - R_A}{1 - R_B} \quad (4)$$

To determine the separation factors with respect to all the solutes, a matrix was formed such that the rows and columns represent the thirteen markers arranged in order of their molecular weight. The separation factors were normalized by the ratio of the molecular weights of the solute pairs to account for the size difference as shown in Eq. (5). This normalized parameter was proposed by Marchetti et al.⁵ and referred to as the selectivity figure of merit ($SFM(\beta_{A/B})$).

$$SFM(\beta_{A/B}) = \frac{\beta_{A/B}}{MW_B/MW_A}, MW_B/MW_A \geq 1 \quad (5)$$

The average selectivity figure of merit (\overline{SFM}) was calculated according to Eq. (6). Any solute that reported a rejection value of 1.0 was excluded from the arithmetic average.

$$\overline{SFM} = \frac{1}{n} \sum_{i=0}^n SFM_{A/B}(\beta) \quad (6)$$

Solubility parameters

The solubility parameters are used to describe the affinity between the polymers, the solutes, and the solvent. The Hansen solubility parameters were calculated using the HSiP software and Eq. (7), where δ_D , δ_P , and δ_H represent the dispersion forces, polar interactions, and hydrogen bonding, respectively⁴⁹. For the polymers, the parameters were calculated for the repeating unit, assuming all reactive groups were consumed during the reaction. Supplementary Table 3 summarizes the Hansen solubility parameters of acetonitrile, solutes⁴⁹, and polymers^{47,49} used in membrane preparation.

$$\delta = \sqrt{(\delta_D)^2 + (\delta_P)^2 + (\delta_H)^2} \quad (7)$$

The distance between compounds A and B in the Hansen space (Ra) was calculated using Eq. (8). If two compounds show good affinity

or solubility, the Ra value is lower than the radius of interaction (Ro). The relative energy difference can be predicted using the ratio of Ra/Ro, the RED number.

$$Ra^2 = 4(\delta_{D,A} - \delta_{D,B})^2 + (\delta_{P,A} - \delta_{P,B})^2 + (\delta_{H,A} - \delta_{H,B})^2 \quad (8)$$

Partitioning coefficient calculations

The partitioning coefficients (LogP) were taken from the PubChem database of the National Library of Medicine⁵⁰. If measured LogP values were not available, the XLogP3 values from the same source were used instead.

Pore size distribution calculations

The pore size distribution calculations were performed according to the literature⁵¹. First, the critical volumes of the solutes were calculated using the Joback group contribution method⁵².

$$V_c = 17.5 + \sum \Delta V_c^i \quad (9)$$

Where $\sum \Delta V_c^i$ is the sum of group contributions for critical volume. From the critical volume, we can calculate the molar volume at the boiling point using the following empirical equation:

$$V_{m,i} = 0.285 \times V_c^{1.048} \quad (10)$$

Using the boiling point molar volume of the solute, the diffusivity coefficient can be calculated from the Wilke-Chang equation:

$$D_{s,j} = 7.4 \times 10^{-4} \frac{T \sqrt{\Phi M}}{\mu_{p,i} V_{m,i}^{0.6}} \quad (11)$$

Where T is the temperature, Φ is the affinity coefficient of the solvent, M is the molar weight of the solvent. $\mu_{p,i}$ is the kinematic viscosity, and V is the molar volume at the boiling point. From the diffusivity coefficient ($D_{s,j}$), we can calculate the equivalent sphere diameter that will have the same diffusivity according to the Stokes-Einstein equation:

$$D_{s,ij} = \frac{KT}{6\pi r_{s,j} \mu_{p,i}} \quad (12)$$

Where K is the Boltzmann constant, r is the radius, and $\mu_{p,i}$ is the matrix (solvent) dynamic viscosity. The resulting radius values can be plotted against the rejection. Then, a generalized logistic function was fitted on the data points, adjusting five parameters according to the equation:

$$g(x) = A + \frac{K - A}{(C + Q \cdot e^{-Bx})^{1/\nu}} \quad (13)$$

The distribution function can be calculated by calculating the derivative of the $g(x)$:

$$g'(x) = \frac{(K - A) \cdot (-B) \cdot Q \cdot e^{-Bx}}{\nu \cdot (C + Q \cdot e^{-Bx})^{\frac{1}{\nu} + 1}} \quad (14)$$

Where A , K , B , Q and ν are internal fitting parameters. The normalized mean expected value of $g'(x)$ is calculated using the numerical integration method on $g'(x)$ after normalization using the scipy's quad function.

Data availability

All data that supports the findings of this study are available within the paper and its supplementary information document. Additional data are available from the corresponding authors upon request.

References

- Nunes, S. P. & Peinemann, K.-V. *Membrane Technology* (Wiley-vch, 2001).
- Marchetti, P., Jimenez Solomon, M. F., Szekely, G. & Livingston, A. G. Molecular separation with organic solvent nanofiltration: A critical review. *Chem. Rev.* **114**, 10735–10806 (2014).
- Vandezande, P., Gevers, L. E. M. & Vankelecom, I. F. J. Solvent resistant nanofiltration: Separating on a molecular level. *Chem. Soc. Rev.* **37**, 365–405 (2008).
- Aristizábal, S. L., Lively, R. P. & Nunes, S. P. Solvent and thermally stable polymeric membranes for liquid molecular separations: Recent advances, challenges, and perspectives. *J. Membr. Sci.* **685**, 121972 (2023).
- Marchetti, P., Peeva, L. & Livingston, A. The selectivity challenge in organic solvent nanofiltration: membrane and process solutions. *Annu. Rev. Chem. Biomol. Eng.* **8**, 473–497 (2017).
- Cadotte, J. E., Petersen, R. J., Larson, R. E. & Erickson, E. E. A new thin-film composite seawater reverse osmosis membrane. *Desalination* **32**, 25–31 (1980).
- Karan, S., Jiang, Z. & Livingston, A. G. Sub-10 nm polyamide nanofilms with ultrafast solvent transport for molecular separation. *Science* **348**, 1347–1351 (2015).
- Jimenez-Solomon, M. F., Song, Q., Jelfs, K. E., Munoz-Ibanez, M. & Livingston, A. G. Polymer nanofilms with enhanced microporosity by interfacial polymerization. *Nat. Mater.* **15**, 760–767 (2016).
- Ali, Z. et al. Finely tuned submicroporous thin-film molecular sieve membranes for highly efficient fluid separations. *Adv. Mater.* **32**, 2001132 (2020).
- He, A. et al. A smart and responsive crystalline porous organic cage membrane with switchable pore apertures for graded molecular sieving. *Nat. Mater.* **21**, 463–470 (2022).
- Yu, S., Yang, M., Liu, Y. & Liu, M. Recent advances in separation membranes based on porous organic molecular materials. *Mater. Chem. Front.* **7**, 3560–3575 (2023).
- Shi, B., Marchetti, P., Peshev, D., Zhang, S. & Livingston, A. G. Will ultra-high permeance membranes lead to ultra-efficient processes? challenges for molecular separations in liquid systems. *J. Membr. Sci.* **525**, 35–47 (2017).
- Huang, T., Alyami, M., Kashab, N. M. & Nunes, S. P. Engineering membranes with macrocycles for precise molecular separations. *J. Mater. Chem. A* **9**, 18102–18128 (2021).
- Huang, T. et al. Molecularly-porous ultrathin membranes for highly selective organic solvent nanofiltration. *Nat. Commun.* **11**, 5882 (2020).
- Huang, T., Puspasari, T., Nunes, S. P. & Peinemann, K.-V. Ultrathin 2D-layered cyclodextrin membranes for high-performance organic solvent nanofiltration. *Adv. Funct. Mater.* **30**, 1906797 (2020).
- Li, X. et al. Polycage membranes for precise molecular separation and catalysis. *Nat. Commun.* **14**, 3112 (2023).
- Villalobos, L. F., Karunakaran, M. & Peinemann, K. V. Complexation-induced phase separation: preparation of composite membranes with a nanometer-thin dense skin loaded with metal ions. *Nano Lett.* **15**, 3166–3171 (2015).
- Jiang, Z. et al. Aligned macrocycle pores in ultrathin films for accurate molecular sieving. *Nature* **609**, 58–64 (2022).
- Pedersen, C. J. The discovery of crown ethers. *Science* **241**, 536–540 (1988).
- Shen, L. et al. Breaking through permeability–selectivity trade-off of thin-film composite membranes assisted with crown ethers. *AIChE J.* **67**, e17173 (2021).
- Li, H. et al. Nanofiltration membrane with crown ether as exclusive Li⁺ transport channels achieving efficient extraction of lithium from Salt Lake Brine. *Chem. Eng. J.* **438**, 135658 (2022).
- Zhao, Y., Song, X., Huang, M., Jiang, H. & Toghan, A. Crown ether interlayer-modulated polyamide membrane with nanoscale structures for efficient desalination. *Nano Res.* **16**, 6153–6159 (2023).
- Jin, X. et al. Crown ether modulated high-performance nanofiltration membrane for water purification. *Chem. Eng. Sci.* **280**, 119064 (2023).
- Shinbo, T., Yamaguchi, T., Nishimura, K. & Sugiura, M. Chromatographic separation of racemic amino acids by use of chiral crown ether-coated reversed-phase packings. *J. Chromatogr. A* **405**, 145–153 (1987).
- Mutihac, L., Mutihac, R., Constantinescu, T. & Luca, C. The transport of amino acids by 18-crown-6 through liquid membranes. *J. Incl. Phenom. Mol. Recognit. Chem.* **17**, 45–51 (1994).
- Buschmann, H. J., Schollmeyer, E. & Mutihac, L. Complexation of amino acid methylesters and amino alcohols by 18-Crown-6 and Benzo-18-crown-6 in methanol. *J. Incl. Phenom. Macrocycl. Chem.* **40**, 199–202 (2001).
- Badis, M., Tomaszewicz, I., Joly, J.-P. & Rogalska, E. Enantiomeric recognition of amino acids by amphiphilic crown ethers in langmuir monolayers. *Langmuir* **20**, 6259–6267 (2004).
- Silverstein, R. M., Webster, F. X. & Kiemle, D. J. *Spectrometric Identification of Organic Compounds* (John Wiley & Sons, 2005).
- Chuyang Tang, Y.-N. K. & James, O. Leckie. effect of membrane chemistry and coating layer on physiochemical properties of thin film composite polyamide RO and NF membranes: I. FTIR and XPS characterization of polyamide and coating layer chemistry. *Desalination* **242**, 149–167 (2009).
- Dulak, M. et al. Water trapped in Dibenzo-18-crown-6: theoretical and spectroscopic (IR, Raman) studies. *Spectrochim. Acta Part A Mol. Biomol. Spectrosc.* **64**, 532–548 (2006).
- Smith, M., Scudiero, L., Espinal, J., McEwen, J.-S. & Garcia-Perez, M. Improving the deconvolution and interpretation of XPS spectra from chars by Ab initio calculations. *Carbon* **110**, 155–171 (2016).
- Johnston, E. E., Bryers, J. D. & Ratner, B. D. Plasma deposition and surface characterization of oligoglyme, dioxane, and crown ether nonfouling films. *Langmuir* **21**, 870–881 (2005).
- Buechner, C. et al. Quantitative characterization of a desalination membrane model system by X-ray photoelectron spectroscopy. *Langmuir* **35**, 11315–11321 (2019).
- Yuan, K. et al. Porphyrin modified UiO-66-NH₂ for highly efficient photoreduction of Cr (VI) under visible light. *Catalysts* **13**, 1073 (2023).
- Hsieh, B., Ettegui, E. & Gao, Y. The surface species of soly(p-phenylene vinylene) and their effects on metal interface formation. *Synth. Met.* **78**, 269–275 (1996).
- Kvande, I. et al. Importance of oxygen-free edge and defect sites for the immobilization of colloidal Pt oxide particles with implications for the preparation of CNF-supported catalysts. *J. Phys. Chem. C* **114**, 1752–1762 (2010).
- Chai, G.-Y. & Krantz, W. B. Formation and characterization of polyamide membranes via interfacial polymerization. *J. Membr. Sci.* **93**, 175–192 (1994).
- Song, Y., Sun, P., Henry, L. L. & Sun, B. Mechanisms of structure and performance controlled thin film composite membrane formation via interfacial polymerization process. *J. Membr. Sci.* **251**, 67–79 (2005).
- Nulens, I., Ben Zvi, A., Vankelecom, I. F. J. & Ramon, G. Z. Re-thinking polyamide thin film formation: how does interfacial destabilization dictate film morphology? *J. Membr. Sci.* **656**, 120593 (2022).
- He, Y., Zhang, Y., Liang, F., Zhu, Y. & Jin, J. Chlorine resistant polyamide desalination membrane prepared via organic-organic interfacial polymerization. *J. Membr. Sci.* **672**, 121444 (2023).

41. Heiranian, M., Fan, H., Wang, L., Lu, X. & Elimelech, M. Mechanisms and models for water transport in reverse osmosis membranes: History, critical assessment, and recent developments. *Chem. Soc. Rev.* **52**, 8455–8480 (2023).
42. Wang, L. et al. Water transport in reverse osmosis membranes is governed by pore flow, not a solution-diffusion mechanism. *Sci. Adv.* **9**, eadf8488 (2023).
43. Thiermeyer, Y., Blumenschein, S. & Skiborowski, M. Solvent dependent membrane-solute sensitivity of OSN membranes. *J. Membr. Sci.* **567**, 7–17 (2018).
44. Schmitt, M. et al. Structural selection by microsolvation: conformational locking of tryptamine. *J. Am. Chem. Soc.* **127**, 10356–10364 (2005).
45. Zeidler, S., Kätzel, U. & Kreis, P. Systematic investigation on the influence of solutes on the separation behavior of a PDMS membrane in organic solvent nanofiltration. *J. Membr. Sci.* **429**, 295–303 (2013).
46. Ignacz, G., Beke, A. K. & Szekeley, G. Data-driven investigation of process solvent and membrane material on organic solvent nanofiltration. *J. Membr. Sci.* **674**, 121519 (2023).
47. Bastin, M., Hendrix, K. & Vankelecom, I. Solvent resistant nanofiltration for acetonitrile based feeds: A membrane screening. *J. Membr. Sci.* **536**, 176–185 (2017).
48. Pérez-Manríquez, L., Aburabi'e, J., Neelakanda, P. & Peinemann, K.-V. Cross-linked PAN-based thin-film composite membranes for non-aqueous nanofiltration. *React. Funct. Polym.* **86**, 243–247 (2015).
49. Hansen, C. M. *Hansen Solubility Parameters: a User's Handbook*. (CRC Press, 2007).
50. Kim, S. et al. PubChem 2023 update. *Nucleic Acids Res.* **51**, D1373–D1380 (2022).
51. Alduraiei, F., Manchanda, P., Pulido, B., Szekeley, G. & Nunes, S. P. Fluorinated thin-film composite membranes for nonpolar organic solvent nanofiltration. *Sep. Purif. Technol.* **279**, 119777 (2021).
52. Joback, K. G. & Reid, R. C. Estimation of pure-component properties from group-contributions. *Chem. Eng. Commun.* **57**, 233–243 (1987).

Acknowledgements

The research reported in this publication was supported by funding from King Abdullah University of Science and Technology (KAUST). We especially thank Thom Leach, a scientific illustrator at KAUST, for creating Fig. 1 and Long Chen for carrying out the AFM experiments.

Author contributions

S.N. and G.S. secured funding, conceived, and supervised the project. B.A. and G.I. designed the experiments. G.I. carried out the monomer

synthesis and characterization. B.A. carried out the membrane fabrication, material characterization, and performance evaluation. B.A. and G.I. analyzed the membrane performance. G.I. devised the selectivity matrix. M.D.V. co-supervised the project and contributed to the spectroscopic analysis. M.H. carried out and analyzed the XPS experiments. All authors discussed the findings and assisted in comprehending the results.

Competing interests

The authors declare no competing interests.

Additional information

Supplementary information The online version contains supplementary material available at <https://doi.org/10.1038/s41467-024-51548-7>.

Correspondence and requests for materials should be addressed to Gyorgy Szekeley or Suzana P. Nunes.

Peer review information *Nature Communications* thanks Yan Wang, Song Zhao, and the other anonymous, reviewer(s) for their contribution to the peer review of this work. A peer review file is available.

Reprints and permissions information is available at <http://www.nature.com/reprints>

Publisher's note Springer Nature remains neutral with regard to jurisdictional claims in published maps and institutional affiliations.

Open Access This article is licensed under a Creative Commons Attribution-NonCommercial-NoDerivatives 4.0 International License, which permits any non-commercial use, sharing, distribution and reproduction in any medium or format, as long as you give appropriate credit to the original author(s) and the source, provide a link to the Creative Commons licence, and indicate if you modified the licensed material. You do not have permission under this licence to share adapted material derived from this article or parts of it. The images or other third party material in this article are included in the article's Creative Commons licence, unless indicated otherwise in a credit line to the material. If material is not included in the article's Creative Commons licence and your intended use is not permitted by statutory regulation or exceeds the permitted use, you will need to obtain permission directly from the copyright holder. To view a copy of this licence, visit <http://creativecommons.org/licenses/by-nc-nd/4.0/>.

© The Author(s) 2024